PCCP

PAPER

View Article Online
View Journal | View Issue

Cite this: *Phys. Chem. Chem. Phys.*, 2017, **19**, 2131

Investigating how vesicle size influences vesicle adsorption on titanium oxide: a competition between steric packing and shape deformation†

Abdul Rahim Ferhan,[a] Joshua A. Jackman[a] and Nam-Joon Cho*[ab]

Understanding the adsorption behavior of lipid vesicles at solid–liquid interfaces is important for obtaining fundamental insights into soft matter adsorbates as well as for practical applications such as supported lipid bilayer (SLB) fabrication. While the process of SLB formation has been highly scrutinized, less understood are the details of vesicle adsorption without rupture, especially at high surface coverages. Herein, we tackle this problem by employing simultaneous quartz crystal microbalance-dissipation (QCM-D) and localized surface plasmon resonance (LSPR) measurements in order to investigate the effect of vesicle size (84–211 nm diameter) on vesicle adsorption onto a titanium oxide surface. Owing to fundamental differences in the measurement principles of the two techniques as well as a mismatch in probing volumes, it was possible to determine both the lipid mass adsorbed near the sensor surface as well as the total mass of adsorbed lipid and hydrodynamically coupled solvent in the adsorbed vesicle layer as a whole. With increasing vesicle size, the QCM-D frequency signal exhibited monotonic behavior reaching an asymptotic value, whereas the QCM-D energy dissipation signal continued to increase according to the vesicle size. In marked contrast, the LSPR-tracked lipid mass near the sensor surface followed a parabolic trend, with the greatest corresponding measurement response occurring for intermediate-size vesicles. The findings reveal that the maximum extent of adsorbed vesicles contacting a solid surface occurs at an intermediate vesicle size due to the competing influences of vesicle deformation and steric packing. Looking forward, such information can be applied to control the molecular self-assembly of phospholipid assemblies as well as provide the basis for investigating deformable, soft matter adsorbates.

Received 20th November 2016,
Accepted 7th December 2016

DOI: 10.1039/c6cp07930j

www.rsc.org/pccp

Introduction

Understanding the physicochemical factors which influence biomacromolecular adsorption at solid–liquid interfaces is important for obtaining insight into the fundamental properties of biomacromolecules as well as enabling control over molecular self-assembly pathways.[1–4] A classic example is the adsorption and rupture of phospholipid vesicles on solid supports such as gold and metal oxides.[5–8] Depending on the experimental conditions, vesicle properties, and solid support, vesicles can adsorb onto the surface and might experience shape deformation due to the vesicle–substrate interaction.[9–12] If vesicle deformation is modest, then the adsorbed vesicles will continue to adsorb until reaching saturation, *i.e.*, a maximum degree of close-packing.[12–14] On the other hand, if vesicle deformation is significant, then it can promote the spontaneous rupture of adsorbed vesicles *via* one or more pathways leading to supported lipid bilayer (SLB) formation.[15–18] While the process of SLB formation has been highly scrutinized, less understood are the details of vesicle adsorption without rupture as it is challenging to dissect the competing factors of vesicle packing and shape deformation at high surface coverages.

To investigate vesicle adsorption alone as well as within the context of SLB formation, a wide variety of surface-sensitive measurement techniques have been utilized, including acoustic sensors such as the quartz crystal microbalance-dissipation (QCM-D)[19,20] sensors as well as optical sensors such as surface plasmon resonance,[7,21–23] reflectometry,[24–26] and ellipsometry sensors.[13,27] QCM-D is sensitive to both adsorbed lipid mass as well as hydrodynamically coupled solvent, which enables a detailed investigation of the mass (lipid plus solvent) and viscoelastic properties of an adsorbed vesicle layer.[8,28] At the same time, QCM-D data interpretation is generally challenging due to model assumptions (*e.g.*, uniform film properties) and hydrodynamic coupling effects,[28–31] and the measurement response is not directly proportional to the surface coverage

[a] *School of Materials Science and Engineering, Nanyang Technological University, 50 Nanyang Avenue 639798, Singapore. E-mail: njcho@ntu.edu.sg*
[b] *School of Chemical and Biomedical Engineering, Nanyang Technological University, 62 Nanyang Drive 637459, Singapore*

† Electronic supplementary information (ESI) available. See DOI: 10.1039/c6cp07930j

of adsorbed particles.[14] By contrast, the aforementioned optical sensors are sensitive to lipid mass only,[32,33] and therefore they are better suited for determining the total number of adsorbed vesicles, while less suited for probing structural configurations. As each measurement technique has its own particular strengths, there has also been interest in conducting simultaneous measurements using QCM-D and an accompanying optical technique in order to obtain more detailed insight into the corresponding structural and hydration properties of adsorbed vesicle layers.[13,24,27] Of note, the existing vesicle adsorption studies that utilize combined measurement systems have involved the pairing of QCM-D with optical sensor techniques that have similar or longer probing volumes, with penetration depths on the order of a few hundred nanometers which exceed the length scale of adsorbed vesicles. As a result, the existing combined measurement approaches have had relatively low sensitivity to the shape deformation of adsorbed vesicles and other related aspects.

One emerging option to study vesicle adsorption and deformation is nanoplasmonic biosensing, typically based on localized surface plasmon resonance (LSPR),[10,34–36] which is another surface-sensitive, optical sensor technique with a much shorter penetration depth in the range of 5 to 20 nm.[37,38] Using the LSPR technique, it has been possible to monitor quantitative aspects of vesicle adsorption as a function of lipid concentration and vesicle size,[35] as well as the effect of temperature on the deformation of fluid-phase and gel-phase lipid vesicles.[34] Importantly, these measurement capabilities have enabled a comparison of the extent of vesicle deformation on different substrates.[39] Moreover, the high surface sensitivity of nanoplasmonic biosensing has also been utilized to detect vesicle rupture based on the observation that adsorbed lipids in an SLB are, on average, closer to the sensor surface than lipids in adsorbed vesicles.[36,40] While LSPR has the merits of studying vesicle deformation within the broader context of understanding more about vesicle adsorption at high coverages, it is difficult to unravel signal responses arising from the total number of adsorbed vesicles *versus* the deformation state of adsorbed vesicles by a single measurement technique alone. In a few cases, simultaneous QCM-D and nanoplasmonic biosensing experiments have been conducted on silica substrates in order to study SLB formation.[41–43] However, to date, combined measurement approaches to investigate vesicle adsorption without rupture have not been explored.

Herein, we investigated the adsorption of zwitterionic 1,2-dioleoyl-*sn-glycero*-3-phosphocholine (DOPC) lipid vesicles onto a titanium oxide surface by performing simultaneous QCM-D and LSPR measurements. The titanium oxide surface was chosen because zwitterionic lipid vesicles do not rupture on this substrate.[8,14] Particular focus was placed on the role of vesicle size, which is known to influence many relevant factors, including the adsorption rate, the extent of deformation, and the packing of adsorbed vesicles due to steric considerations.[8,31,35,39,44] With increasing vesicle size, the QCM-D responses became less sensitive to vesicle size whereas the LSPR response showed a maximum signal, corresponding to the greatest extent of lipid mass in contact with the sensor surface, for intermediate-size vesicles. Importantly, these findings reveal an interplay between vesicle deformation and vesicle packing that is strongly influenced by the vesicle size and support the suggestion that there is an optimal vesicle size for coating the sensor surface with adsorbed vesicle layers.

Experimental section

Lipid vesicles

Vesicles composed of 1,2-dioleoyl-*sn-glycero*-3-phosphocholine (DOPC) (Avanti Polar Lipids, Alabaster, AL) were prepared by the extrusion method.[45] The DOPC lipid has a gel-to-fluid phase transition temperature of −17 °C, and therefore the resulting vesicles are in the fluid-phase state at room temperature.[46] Briefly, lipids dissolved in chloroform were treated with a stream of nitrogen gas to form a dried lipid film. The film was rehydrated in aqueous buffer solution (10 mM Tris [pH 7.5] with 150 mM NaCl) at a nominal lipid concentration of 5 mg mL^{-1}, followed by vortexing. Extrusion was then performed using an Avanti Mini-Extruder with track-etched polycarbonate membranes with diameters of 50, 80, 100, or 200 nm to produce vesicles with different average sizes. Vesicles were diluted in buffer solution immediately before experiment and used within 24 h of preparation. All aqueous solutions and buffers were prepared with Milli-Q-treated water with a minimum resistivity of 18.2 MΩ cm (Millipore, Billerica, MA).

Dynamic light scattering

Dynamic light scattering (DLS) was performed on a 90Plus particle size analyzer, and the results were analyzed using digital autocorrelator software (Brookhaven Instruments Corporation, New York, USA). All measurements were taken at a scattering angle of 90° where the reflection effect is minimized, and vesicle sizes are reported as the average diameter.

Measurement setup

The combined QCM-D and LSPR setup is comprised of the Q-Sense E1 system (Biolin Scientific, Stockholm, Sweden) together with the Insplorion Acoulyte (Insplorion AB, Gothenburg, Sweden), which provides an optical connection between the QCM-D measurement chamber and the Insplorion X-Nano optics unit (Insplorion AB, Gothenburg, Sweden). Measurements were performed on the Acoulyte quartz crystal sensor, which is a modified version of the regular Q-Sense quartz crystal sensor whereby the top electrode is coated with a silicon dioxide spacer layer on which randomly distributed gold nanodisks (height and diameter of ~20 and ~100 nm, respectively) were fabricated by hole–mask colloidal lithography[47] and sputter-coated with a thin layer of titanium oxide (thickness ~10 nm). Prior to use, the sensor was soaked in a 1% v/v sodium dodecyl sulfate (SDS) solution for 30 min, and then rinsed with water and ethanol, respectively. After drying with a stream of nitrogen gas, the sensor was cleaned using an oxygen plasma cleaner for at least 30 s, before immediately fixing the treated sensor chip in the Q-Sense QWM401 window module, which was then

mounted in the E1 chamber. The solution outlet was connected to a Reglo Digital peristaltic pump (Ismatec, Glattbrugg, Switzerland) in order to control the introduction of fluid samples. Samples were introduced under continuous flow at a flow rate of 100 μL min^{-1}. The window module provides optical access to the sensor *via* the branched fiber probe of the Acoulyte adaptor, which is comprised of connectors to the lamp and the spectrometer (both contained within the Insplorion X-Nano optics unit), which join to form the probe end of the fiber.

Data analysis

QCM-D data analysis was performed using the Voigt–Voinova model available in the Q-Tools software package (Biolin Scientific). For the model fitting, the thickness and effective acoustic mass of the adsorbed vesicle layer were calculated by assuming the film density to be 1000 kg m^{-3} and the viscosity of the bulk aqueous solution to be 0.001 Pa s^{-1}.[24] The LSPR data analysis was performed using the Insplorer software package (Insplorion AB). The time resolution was 1 Hz. The spectral resolution of the plasmon resonance was determined by high-order polynomial fitting, and the centroid position, which is denoted as the LSPR peak position in this work, was calculated from the fit.[48]

Results and discussion

Measurement scheme

Our experimental strategy involves simultaneous QCM-D and LSPR measurements on the same titanium oxide-coated substrate in order to monitor vesicle adsorption. A schematic illustration of the detection scheme is presented in Fig. 1A. As the LSPR penetration depth of LSPR (~5–10 nm) is around an order of magnitude shorter than the QCM-D penetration depth (~60–250 nm), the two measurement techniques provide complementary information about the vesicle adsorption process.

The sensor substrate is a conventional QCM-D quartz crystal sensor chip upon which a layer of gold nanodisks was fabricated by hole–mask colloidal lithography, followed by titanium oxide coating. The AT-cut quartz crystal is a piezoelectric material and, when an alternating current is applied between the top and bottom electrodes, a standing acoustic shear wave is generated with a resonance frequency of oscillation.[19,49] When biomacromolecules adsorb onto the sensor surface, the QCM-D responses detect a negative change in the resonance frequency, which is related to the acoustic mass of the adsorbate (biomacromolecule and hydrodynamically coupled solvent), as well as a typically positive change in energy dissipation that is related to the viscoelastic properties of the adsorbate.[29,49]

Concurrently, the LSPR measurement signal also tracks the adsorption process, and this optical response originates from the interaction of light with the gold nanodisks, which leads to a resonant oscillation of conducting electrons that are locally confined to the surface.[50] Specifically, there is light extinction over a wavelength range, as characterized by the extinction spectra, with maximum extinction occurring at the resonant wavelength, λ_{max}. The measurement response, including the wavelength at which the maximum extinction occurs, is sensitive to the refractive index in the near-vicinity of the gold nanodisk surface.[51] When a vesicle adsorbs onto the nanodisk surface, there is an increase in the local refractive index because biomacromolecules have a larger refractive index than aqueous solvent, and as a result there is a red-shift in the extinction spectra that corresponds to $\Delta\lambda_{max}$. In our measurement configuration, the LSPR signal is obtained in reflection mode, and therefore light passes through the nanoplasmonic sensing layer twice before reaching the spectrometer, which results in higher peak extinction and sensitivity.[37,52,53] Representative LSPR spectra before and after adsorption of lipid vesicles are shown in Fig. 1B, indicating the red-shift as expected.

Effect of vesicle size

Using this platform, we next investigated the effect of vesicle size on the vesicle adsorption process. Dynamic light scattering measurements indicated that the average, intensity-weighted effective diameters of the different vesicle populations were 84, 136, 166 and 211 nm, respectively (Fig. S1, ESI†). The QCM-D and LSPR measurement signals, which were collectively obtained in simultaneous measurements, are individually presented in Fig. 2A–C. In all cases, the initial rates of change in the signals decrease with increasing vesicle size, which is expected because

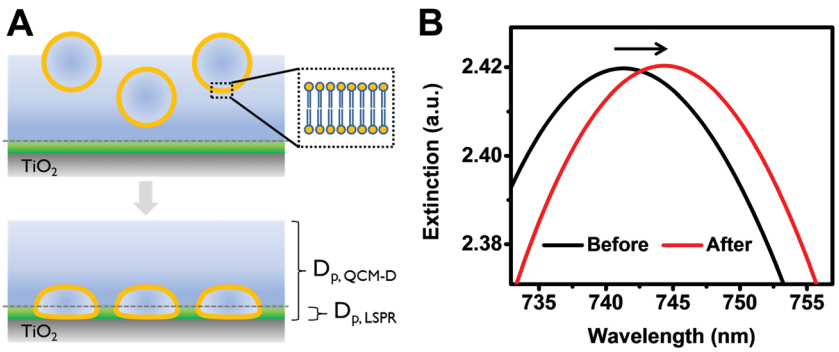

Fig. 1 (A) Schematic illustration of vesicle adsorption onto titanium oxide sensor surfaces, with representative length scales of the penetration depths (D_p) of the QCM-D and LSPR measurement techniques. (B) LSPR extinction spectra before (black) and after (red) the adsorption of DOPC lipid vesicles onto a titanium oxide-coated surface.

the rate of vesicle adsorption is limited by the diffusion of vesicles in bulk solution and larger vesicles diffuse more slowly. However, the final asymptotic values of each signal exhibited different trends with respect to vesicle size. For the QCM-D frequency shifts, the asymptotic values increased sharply from −140 to −200 HZ when the vesicle diameter increased from 84 to 136 nm but remained largely unchanged for larger vesicle sizes (Fig. 2A). By contrast, with increasing vesicle size, the QCM energy dissipation signal also increased from 14 to 37 $\times$ 10^{-6} (Fig. 2B). In the case of 84 nm diameter vesicles only, overshoot behavior was observed in the QCM-D signals, which can be attributed to vesicles adsorbing on top of the nanodisk surfaces and having higher spatial freedom to rock.[33] Of note, this is the only case where the vesicle size was smaller than the nanodisk diameter (~100 nm), and no overshoot behavior was observed for larger vesicles. Voigt–Voinova model analysis of the QCM-D measurement responses indicated that the effective adlayer thickness only increased subtly with greater vesicle size, supporting that larger vesicles deform to a greater extent[44] (Fig. S2, ESI†).

Interestingly, the final asymptotic values of the LSPR signal indicate that, among the tested vesicle sizes, intermediate-size vesicles induced larger peak shifts than smaller or larger vesicles. The 84 and 211 nm diameter vesicles induced peak shifts of 2.6 nm, whereas 136 and 166 nm diameter vesicles led to peak shifts of around 3.0 nm (Fig. 2C). Upon a closer look, this trend in fact agrees well with observations made in our previous work with transmission-mode LSPR measurements for vesicles in this size range.[35] While scaling laws for the adsorption of spherical vesicles predict that, at saturation, smaller vesicles would lead to a larger peak shift,[35] it appears that there is a deviation of >100 nm diameters, likely due to two factors, deformation of adsorbed vesicles and the influence of vesicle size on packing coverage.

As such, the QCM-D and LSPR measurement signals reveal different trends with increasing vesicle size, and the final saturation values for different signals are plotted as a function of vesicle size in Fig. 2D. These different trends underscore the benefits of combining multiple measurement techniques with different surface sensitivities in order to reveal new information about how vesicle size influences vesicle adsorption. Based on the experimental results, it appears that intermediate-size vesicles have the greatest contact with the sensor surface and this is likely due to an optimal balance of high packing and shape deformation.

Vesicle adsorption kinetics

We next investigated the kinetics of vesicle adsorption, and note that both the QCM-D and LSPR responses took longer to stabilize with increasing vesicle size, which is expected due to diffusion-limited adsorption.[31,35,54] In order to compare the different measurement responses, we directly evaluated the rate of acoustic (QCM-D) and optical (LSPR) mass uptake based on normalized curves (Fig. 3A–D). In all cases, the initial linear rate of increase in the frequency shift agreed well with the rate of increase in the LSPR peak shift, before the two signals started to deviate and eventually reached saturation at different time points. For 84 nm diameter vesicles, overshooting in the

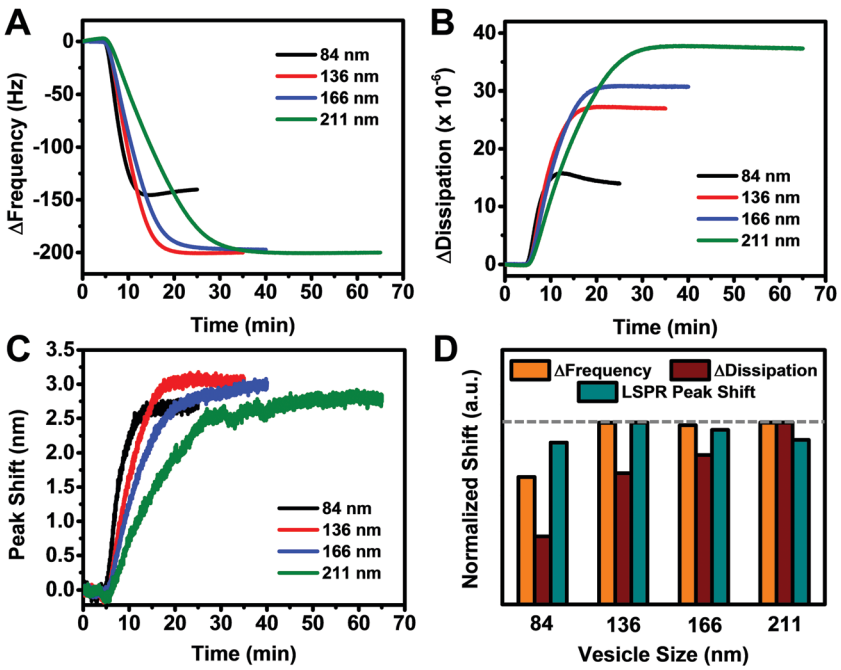

Fig. 2 Temporal variation of QCM-D (A) frequency and (B) dissipation shifts as well as (C) LSPR peak shifts obtained simultaneously during the adsorption of vesicles of different sizes. (D) Plot of final changes in the frequency, dissipation and peak shift values as a function of vesicle size. Measurement data have been normalized such that the highest observed shift detected by each technique is equal to 1. The horizontal dashed line serves as a guide to the eye to the highest observed shifts.

frequency shift occurred around 5 min before the LSPR peak shift stabilized (Fig. 3A). Viewed collectively, the overshooting indicates a decrease in the hydrodynamically coupled solvent as additional vesicles adsorb onto the surface and displace a portion of solvent between adsorbed vesicles.

By contrast, for 136 nm diameter vesicles, the kinetics of the frequency shift closely match those of the LSPR peak shift almost throughout the entire process, suggesting that the rates of acoustic and optical mass uptake are similar (Fig. 3B). However, with increasing vesicle size, for 166 nm diameter vesicles, the frequency shift again stabilized earlier than the LSPR peak shift (Fig. 3C). A similar trend was also observed for 211 nm diameter vesicles, and the difference in the time scale between stabilization of the two signals was even more appreciable, suggesting an increased role of coupled solvent and steric effects for large vesicles (Fig. 3D). The combination of simultaneous QCM-D and LSPR measurements allows the vesicle adsorption process to be temporally separated into three measurement stages characterized by when the rate of change in the QCM-D frequency shift matches that of the LSPR peak shift (stage 1), there is a deviation between the two signals before stabilization of the QCM-D frequency shift is reached (stage 2), and subsequent progression until stabilization of the LSPR peak shift is reached (stage 3). As such, stage 3 represents vesicle adsorption at very high surface coverages, a regime which cannot be detected by QCM-D measurement alone due to hydrodynamic coupling between neighboring vesicles and associated steric effects.

Time-independent vesicle adsorption behavior

In order to evaluate the relative contribution of steric effects as the adsorption process continues at higher surface coverages, we examined the structural properties of the adlayer as a function of vesicle size through time-independent QCM-D frequency *versus* dissipation (f–D) curves.[8,31] The f–D curves show steeper gradients with increasing size, which generally implies a higher increase in energy dissipation per adsorbing vesicle (Fig. 4A). This can be further attributed to a higher amount of solvent coupled to larger vesicles as evidenced by the curves of the QCM-D frequency shift *versus* LSPR peak shift (λ–f curves), which gradually become steeper and progressively overlap with increasing size (Fig. 4B). The increase in coupled solvent contribution to the acoustic mass becomes gradually diminished with increasing optical mass, leading to no further change in the gradient of the λ–f curve at some point. In addition, larger vesicles are prone to greater deformation[23,31] and are less efficiently packed, resulting in greater viscoelastic contribution per adsorbing vesicle, as reflected in the energy dissipation response described above. This is further evidenced by plots of the QCM-D energy dissipation response *versus* the LSPR peak shift (λ–D curves) (Fig. 4C), which also become steeper with increasing vesicle size but without overlapping, suggesting that unlike frequency shifts, the dissipation shifts are mainly determined by the packing arrangement of the vesicles instead of a hydrodynamically coupled solvent.

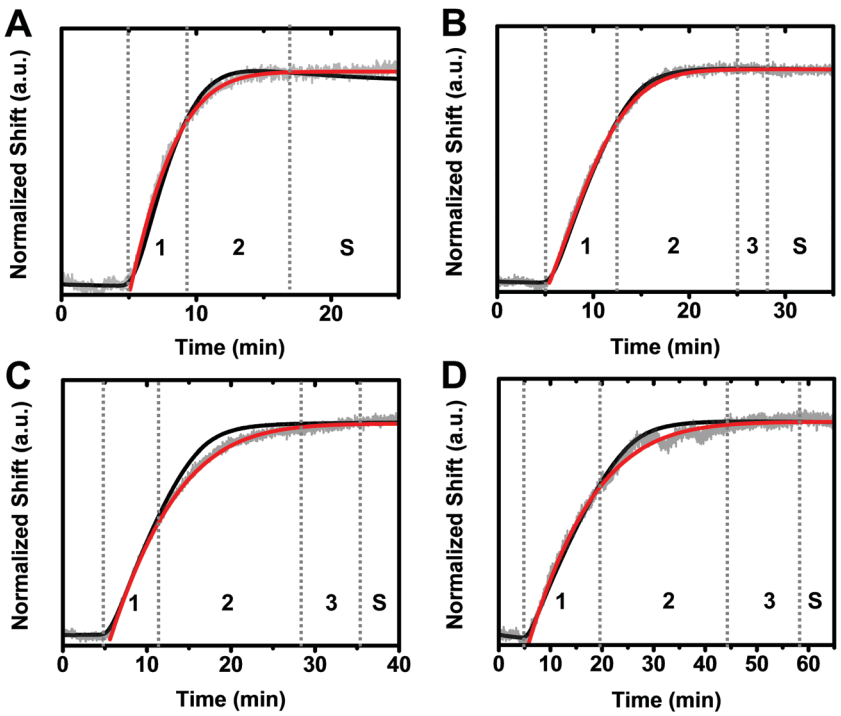

Fig. 3 Normalized QCM-D frequency shifts (black traces) superimposed against normalized LSPR peak shifts (grey traces) obtained simultaneously during the adsorption of DOPC vesicles with (A) 84 nm, (B) 136 nm, (C) 166 nm and (D) 211 nm diameter. A Gaussian function is applied to fit the LSPR peak shifts (red traces, $R^2 > 0.99$ in all cases). The adsorption process can be separated into 3 stages as denoted by the vertical dashed lines and characterized by (1) variations in the QCM-D frequency shift that matches the LSPR peak shift, (2) deviation in the two signals before a stabilized QCM-D frequency shift is reached and (3) subsequent progression before a stabilized LSPR peak shift is reached, (S) before both signals eventually stabilize.

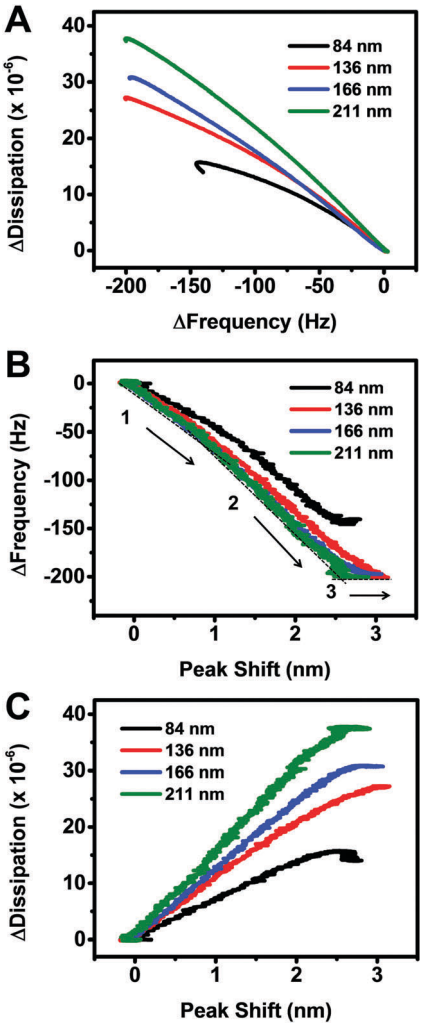

Fig. 4 (A) The time-independent QCM-D frequency–dissipation curves (f–D curves), particularly highlighting the increasing contribution of larger vesicles to adlayer viscoelasticity. (B) The correlation between wet and dry mass changes is inferred from the plot of QCM-D frequency shift *versus* LSPR peak shift (λ–f curves) characterized by a change in gradient from (1) to (2) and a further peak shift after the frequency shift has stabilized (3). (C) Structural transformations observable through the time-independent plot of QCM-D dissipation shifts *versus* LSPR peak shift (λ–D curves).

The λ–f curve also showed a subtle increase in the gradient at a peak shift of $\sim$1 nm for all vesicle sizes, suggesting an increase in the amount of coupled solvent per adsorbing vesicle. This occurs because the number of adsorbed vesicles reaches a sufficiently high coverage at which there is an overlap of the coupled solvent between vesicles leading to a complete-spanning, adsorbed layer of vesicles and coupled solvent across the surface. The increase in the gradient of the λ–f curve is followed by a small increase in the LSPR peak shift while the frequency signal remains stable. Similarly, the λ–D curves also show a brief increase in the LSPR peak shift while the energy dissipation signal remains stable. These trends arise from the fact that the QCM-D responses saturate before the maximum effective surface coverage is achieved, which agrees well with previous findings by Reviakine *et al.*[14] Here, we observe that the LSPR signal and its probing of lipid mass accumulation near the sensor surface continues even after the acoustic mass response has stabilized, allowing greater scrutiny into the final stage of intact vesicle adsorption up to maximum surface coverage. In particular, the λ–f and λ–D plots show that this stage gradually becomes more pronounced for larger vesicles, suggesting its important role in determining the overall kinetics of the adsorption process as vesicle size increases.

Stage-wise description of the vesicle adsorption process

Based on the comparison of temporal variations in the QCM-D frequency shifts and LSPR peak shifts as well as observations from the λ–f and λ–D curves, the competition between steric packing and vesicle deformation during the adsorption of intact vesicles on titanium oxide is explained by describing the process in three stages, as seen in the schematic illustration of Fig. 5. The first stage involves vesicle adsorption at a relatively low surface coverage and minimal coupled solvent between adsorbed vesicles. The second stage involves continued addition of adsorbed vesicles, and hydrodynamic coupling between vesicles becomes more pronounced at higher surface coverages. With increasing size, steric effects also become more prominent at this stage, due to greater deformation as well as lower packing efficiency (“steric effect”). The third stage involves the displacement of the coupled solvent by additional vesicles, which is detected by the LSPR technique only, while the QCM-D responses maintain constant responses. At this stage, steric effects are particularly pronounced due to the relatively poor packing efficiency of larger vesicles.

Since the effect of steric packing is most prominent at high surface coverages, we pay particular attention to the third stage that is undetectable using the QCM-D technique. By comparing the times at which the QCM-D frequency and LSPR peak shift stabilize, it was determined that the length of time of the third stage was around 3, 8 and 17 minutes for 136, 166 and 211 nm diameter vesicles, respectively (Fig. S3, ESI†). Hence, it is more difficult to form close-packed vesicle adlayers on titanium oxide with larger vesicles due to greater deformation and lower packing efficiency. These findings are reminiscent of our previous findings that steric hindrance hinders SLB formation on silicon oxide.[39] Along these lines, it is noteworthy that our earlier discussions on steric effects have been limited to the context of vesicle rupture leading to SLB formation on silicon dioxide surfaces and have been largely inferred from QCM-D measurements.[39,55] As such, these previous efforts concentrated on steric effects at appreciably lower surface coverages. By contrast, the present work presents the first detailed characterization of the steric effect contribution, presenting direct evidence that is consistent with the observations, and supports the claims, of our previous results, while extending the applicability of the “steric effect” concept to adsorbed vesicles that remain intact and at much higher surface coverages up to saturation.

A summary of how vesicle size affects vesicle adsorption in terms of packing considerations and shape deformation is illustrated in Fig. 6. With an initial increase in vesicle size (*i.e.*, from 84 to 136 nm diameter), greater deformability

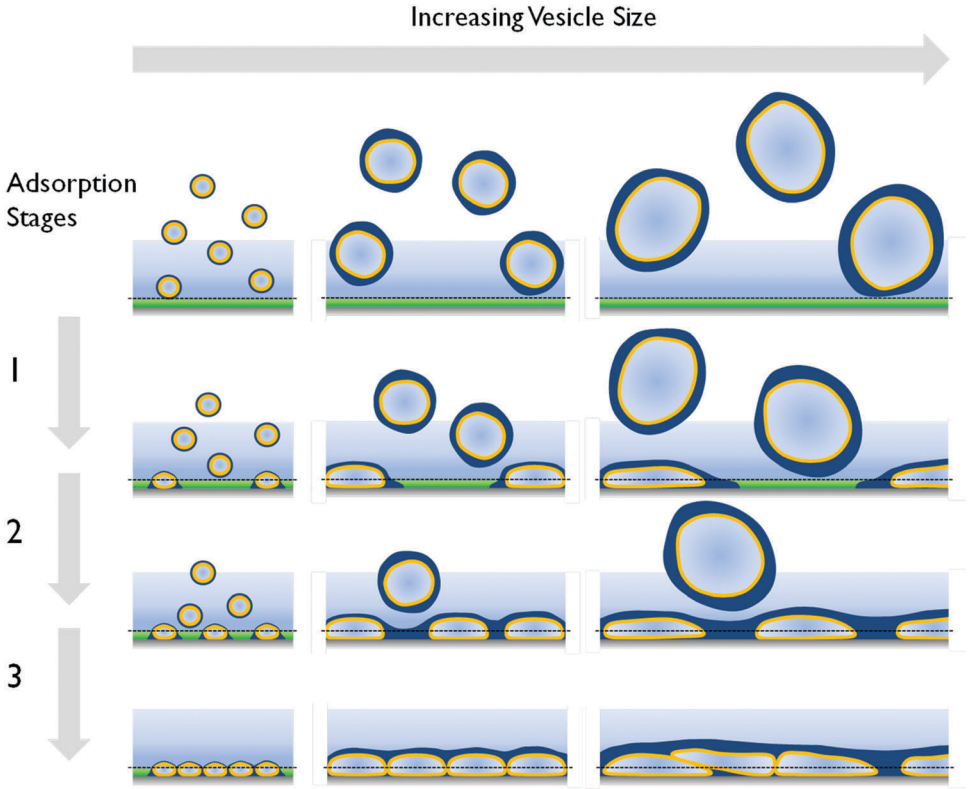

Fig. 5 Schematic illustration of how vesicle size influences vesicle adsorption. The three stages in the adsorption of different-size intact vesicles on titanium oxide, superimposed against the penetration depths of QCM-D (light blue region) and LSPR (green region below the dashed line); hydrodynamically-coupled solvent is included in the schematic drawing (dark blue shade). Stages 1 & 2 correspond to linear correlations between the frequency and the LSPR peak shift that show slightly different gradients (in λ–f plot), while stage 3 is reflected by frequency- and dissipation-independent LSPR peak shifts (in λ–f and λ–D plots). Stage 3 corresponds to further vesicle adsorption while the acoustic mass remains unchanged, and this effect is more pronounced for larger vesicles.

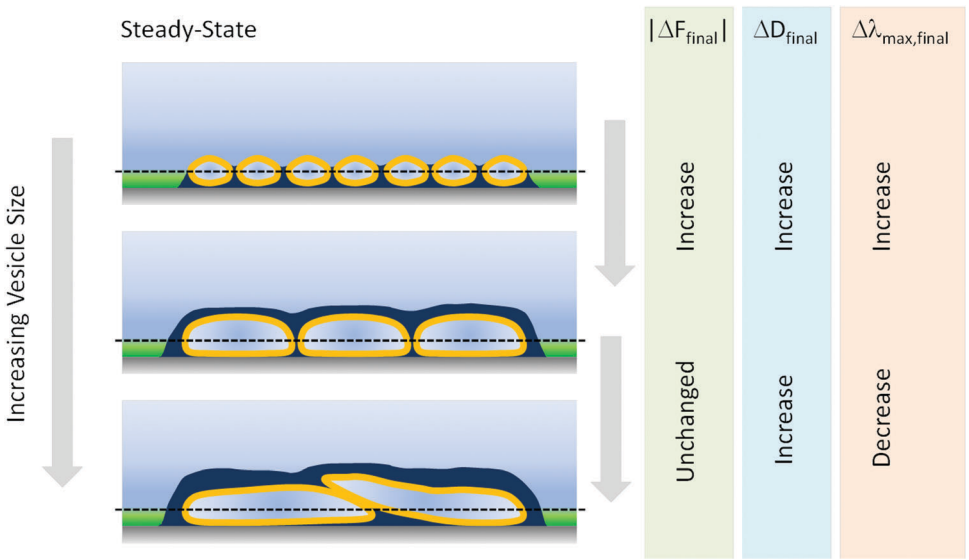

Fig. 6 Simplified schematic of the final configuration of adsorbed vesicles with increasing size superimposed against the penetration depths of QCM-D (light blue region) and LSPR (green region below the dashed line). With increasing size, the vesicles deform to a greater extent. At the same time, the amount of coupled solvent (dark blue region) contribution to the resulting continuous film increases to a certain extent before it saturates, consequently reducing the steric packing on the substrate. This results in ΔF_{final}, ΔD_{final}, and $\Delta\lambda_{max,final}$ varying with different trends, with increasing vesicle size.

promotes vesicle flattening so that lipids are, on average, nearer to the sensor surface, resulting in higher saturation values of the LSPR signal. At the same time, with increasing vesicle size, there is again a drop in the maximum LSPR peak shift because the maximum packing coverage of adsorbed vesicles becomes lower due to steric effects. By contrast, the QCM-D frequency shift is largely insensitive to the size of adsorbed vesicles while the QCM-D energy dissipation signal increases with greater vesicle size. Based on the different measurement responses, we have identified that vesicle size influences vesicle adsorption *via* two competing factors, vesicle deformation and steric effects on packing. Moreover, our measurement results indicate that an optimal balance of these two factors is achieved for intermediate-size vesicles.

Conclusion

The effect of vesicle size (84–211 nm diameter) on vesicle adsorption onto a titanium oxide surface was investigated by simultaneous QCM-D and LSPR measurements. By tracking the total mass of adsorbed lipid and hydrodynamically coupled solvent in the adsorbed vesicle layer as well as lipid mass adsorbed near the sensor surface, we were able to characterize vesicle adsorption without rupture even after the QCM-D signals have saturated, revealing continued vesicle adsorption behavior up to higher surface coverages. In this regime, vesicle adsorption is predominantly governed by steric packing, which competes with vesicle deformation in determining the effect of vesicle size on the overall degree of vesicle contact with the adsorbing surface. With increasing vesicle size, although higher deformability leads to higher surface contact by individual vesicles, steric effects reduce their packing efficiency, resulting in lower overall contact at saturation. The maximum extent of adsorbed vesicles contacting a solid surface therefore occurs at an intermediate vesicle size. This is manifested by QCM-D frequency signals that increased monotonically reaching saturation, QCM-D dissipation signals that increased almost linearly and, in contrast, LSPR peak shifts that followed a parabolic trend, with the greatest value occurring for intermediate-sized vesicles (136 nm diameter in our experiments). As seen in this work, the characterization of vesicle adsorption in the high surface coverage regime provides the basis for a deeper understanding of how steric effects contribute to the molecular self-assembly of phospholipid assemblies as well as play a role in the behavior of soft-matter adsorbates in general.

Acknowledgements

This work was supported by a National Research Foundation Proof-of-Concept Grant (NRF2015NRF-POC001-019).

References

1 A. E. Nel, L. Madler, D. Velegol, T. Xia, E. M. V. Hoek, P. Somasundaran, F. Klaessig, V. Castranova and M. Thompson, *Nat. Mater.*, 2009, **8**, 543–557.
2 M. A. Cole, N. H. Voelcker, H. Thissen and H. J. Griesser, *Biomaterials*, 2009, **30**, 1827–1850.
3 T. M. Squires, R. J. Messinger and S. R. Manalis, *Nat. Biotechnol.*, 2008, **26**, 417–426.
4 B. Kasemo, *Surf. Sci.*, 2002, **500**, 656–677.
5 G. J. Hardy, R. Nayak and S. Zauscher, *Curr. Opin. Colloid Interface Sci.*, 2013, **18**, 448–458.
6 I. Czolkos, A. Jesorka and O. Orwar, *Soft Matter*, 2011, **7**, 4562–4576.
7 E. Reimhult, M. Zäch, F. Höök and B. Kasemo, *Langmuir*, 2006, **22**, 3313–3319.
8 E. Reimhult, F. Höök and B. Kasemo, *J. Chem. Phys.*, 2002, **117**, 7401–7404.
9 M. Dacic, J. A. Jackman, S. Yorulmaz, V. P. Zhdanov, B. Kasemo and N.-J. Cho, *Langmuir*, 2016, **32**, 6486–6495.
10 J. A. Jackman, B. Spackova, E. Linardy, M. C. Kim, B. K. Yoon, J. Homola and N.-J. Cho, *Chem. Commun.*, 2016, **52**, 76–79.
11 J. A. Jackman, J.-H. Choi, V. P. Zhdanov and N.-J. Cho, *Langmuir*, 2013, **29**, 11375–11384.
12 I. Reviakine, M. Gallego, D. Johannsmann and E. Tellechea, *J. Chem. Phys.*, 2012, **136**, 084702.
13 J. A. Jackman, G. H. Zan, Z. Zhao and N.-J. Cho, *Langmuir*, 2014, **30**, 5368–5372.
14 I. Reviakine, F. F. Rossetti, A. N. Morozov and M. Textor, *J. Chem. Phys.*, 2005, **122**, 204711.
15 R. P. Richter, R. Bérat and A. R. Brisson, *Langmuir*, 2006, **22**, 3497–3505.
16 R. Richter, A. Mukhopadhyay and A. Brisson, *Biophys. J.*, 2003, **85**, 3035–3047.
17 J. M. Johnson, T. Ha, S. Chu and S. G. Boxer, *Biophys. J.*, 2002, **83**, 3371–3379.
18 V. P. Zhdanov and B. Kasemo, *Langmuir*, 2001, **17**, 3518–3521.
19 M. C. Dixon, *Journal of Biomolecular Techniques: JBT*, 2008, **19**, 151–158.
20 F. Höök, M. Rodahl, P. Brzezinski and B. Kasemo, *Langmuir*, 1998, **14**, 729–734.
21 S. H. Kristensen, G. A. Pedersen, L. N. Nejsum and D. S. Sutherland, *J. Phys. Chem. B*, 2013, **117**, 10376–10383.
22 E. Reimhult, C. Larsson, B. Kasemo and F. Höök, *Anal. Chem.*, 2004, **76**, 7211–7220.
23 C. A. Keller, K. Glasmästar, V. P. Zhdanov and B. Kasemo, *Phys. Rev. Lett.*, 2000, **84**, 5443–5446.
24 N.-J. Cho, G. Wang, M. Edvardsson, J. S. Glenn, F. Hook and C. W. Frank, *Anal. Chem.*, 2009, **81**, 4752–4761.
25 M. Edvardsson, S. Svedhem, G. Wang, R. Richter, M. Rodahl and B. Kasemo, *Anal. Chem.*, 2009, **81**, 349–361.
26 G. Wang, M. Rodahl, M. Edvardsson, S. Svedhem, G. Ohlsson, F. Höök and B. Kasemo, *Rev. Sci. Instrum.*, 2008, **79**, 075107.
27 G. H. Zan, J. A. Jackman and N.-J. Cho, *J. Phys. Chem. B*, 2014, **118**, 3616–3621.
28 C. A. Keller and B. Kasemo, *Biophys. J.*, 1998, **75**, 1397–1402.
29 N.-J. Cho, C. W. Frank, B. Kasemo and F. Höök, *Nat. Protoc.*, 2010, **5**, 1096–1106.
30 N.-J. Cho, K. K. Kanazawa, J. S. Glenn and C. W. Frank, *Anal. Chem.*, 2007, **79**, 7027–7035.
31 E. Reimhult, F. Höök and B. Kasemo, *Langmuir*, 2003, **19**, 1681–1691.

32 R. Konradi, M. Textor and E. Reimhult, *Biosensors*, 2012, **2**, 341.
33 I. Reviakine, D. Johannsmann and R. P. Richter, *Anal. Chem.*, 2011, **83**, 8838–8848.
34 E. Oh, J. A. Jackman, S. Yorulmaz, V. P. Zhdanov, H. Lee and N.-J. Cho, *Langmuir*, 2015, **31**, 771–781.
35 J. A. Jackman, V. P. Zhdanov and N.-J. Cho, *Langmuir*, 2014, **30**, 9494–9503.
36 G. H. Zan, J. A. Jackman, S.-O. Kim and N.-J. Cho, *Small*, 2014, **10**, 4828–4832.
37 J. N. Anker, W. P. Hall, O. Lyandres, N. C. Shah, J. Zhao and R. P. Van Duyne, *Nat. Mater.*, 2008, **7**, 442–453.
38 E. Hutter and J. H. Fendler, *Adv. Mater.*, 2004, **16**, 1685–1706.
39 J. A. Jackman, M. C. Kim, V. P. Zhdanov and N.-J. Cho, *Phys. Chem. Chem. Phys.*, 2016, **18**, 3065–3072.
40 M. P. Jonsson, P. Jönsson, A. B. Dahlin and F. Höök, *Nano Lett.*, 2007, **7**, 3462–3468.
41 E. M. Larsson, M. E. M. Edvardsson, C. Langhammer, I. Zorić and B. Kasemo, *Rev. Sci. Instrum.*, 2009, **80**, 125105.
42 A. B. Dahlin, P. Jönsson, M. P. Jonsson, E. Schmid, Y. Zhou and F. Höök, *ACS Nano*, 2008, **2**, 2174–2182.
43 M. P. Jonsson, P. Jönsson and F. Höök, *Anal. Chem.*, 2008, **80**, 7988–7995.
44 K. Dimitrievski, *Langmuir*, 2010, **26**, 3008–3011.
45 F. Olson, C. A. Hunt, F. C. Szoka, W. J. Vail and D. Papahadjopoulos, *Biochim. Biophys. Acta, Biomembr.*, 1979, **557**, 9–23.
46 A. S. Ulrich, M. Sami and A. Watts, *Biochim. Biophys. Acta, Biomembr.*, 1994, **1191**, 225–230.
47 H. Fredriksson, Y. Alaverdyan, A. Dmitriev, C. Langhammer, D. S. Sutherland, M. Zäch and B. Kasemo, *Adv. Mater.*, 2007, **19**, 4297–4302.
48 A. B. Dahlin, J. O. Tegenfeldt and F. Höök, *Anal. Chem.*, 2006, **78**, 4416–4423.
49 M. Rodahl, F. Hook, C. Fredriksson, C. A. Keller, A. Krozer, P. Brzezinski, M. Voinova and B. Kasemo, *Faraday Discuss.*, 1997, **107**, 229–246.
50 K. A. Willets and R. P. V. Duyne, *Annu. Rev. Phys. Chem.*, 2007, **58**, 267–297.
51 V. Häfele, A. Trügler, U. Hohenester, A. Hohenau, A. Leitner and J. R. Krenn, *Opt. Express*, 2015, **23**, 10293–10300.
52 O. Kedem, A. Vaskevich and I. Rubinstein, *J. Phys. Chem. C*, 2014, **118**, 8227–8244.
53 T. Endo, K. Kerman, N. Nagatani, H. M. Hiepa, D. K. Kim, Y. Yonezawa, K. Nakano and E. Tamiya, *Anal. Chem.*, 2006, **78**, 6465–6475.
54 V. P. Zhdanov, C. A. Keller, K. Glasmästar and B. Kasemo, *J. Chem. Phys.*, 2000, **112**, 900–909.
55 J. A. Jackman, Z. Zhao, V. P. Zhdanov, C. W. Frank and N.-J. Cho, *Langmuir*, 2014, **30**, 2152–2160.